POLITECNICO DI TORINO
Repository ISTITUZIONALE

Investigation of process parameters for solar fuel production using earth-abundant materials

(Article begins on next page)
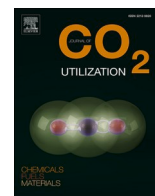
29 June 2024

Investigation of process parameters for solar fuel production using earth-abundant materials

Ashween Kaur Virdee [a,b,*], Irene Martin [c], Jeannie Z.Y. Tan [a,b], Giulia Forghieri [c], M. Mercedes Maroto-Valer [a,b], Michela Signoretto [c], Mijndert Van der Spek [a,b], John M. Andresen [a,b]

[a] *Research Centre for Carbon Solutions (RCCS), Heriot-Watt University, Edinburgh EH14 4AS, United Kingdom*
[b] *Industrial Decarbonisation Research and Innovation Centre (IDRIC), Heriot-Watt University, Edinburgh EH14 4AS, United Kingdom*
[c] *Department of Molecular Sciences and Nanosystems, Ca' Foscari University of Venice and INSTM RU of Venice, via Torino 155, 30172 Venice, Italy*

ABSTRACT

Photoreduction of CO_2 to solar fuels and chemicals offers a sustainable method to produce net zero energy vectors. For large-scale applications, it is crucial to develop an improved understanding of the influence of reaction conditions on the design and optimisation of the photoreactor. The performance of CuO impregnated on $BaTiO_3$ photocatalyst was investigated and compared to pristine $BaTiO_3$, and CuO impregnated on commercial P25 (CuO/P25) and ZnO. The influence of irradiance, CO_2 and H_2O flow and partial pressure, and CO_2/H_2O ratio on the product yield and selectivity were examined. Using Design of Experiments and Computational Fluid Dynamic modelling, the optimised reaction conditions were irradiance of 125 mW cm^{-2}, with a CO_2 flow of 0.09 mL min^{-1}, and water bubbler temperature of 25 °C. At these conditions, a 2 and 10-fold increase of CO and CH_4 production, respectively, were obtained, compared to baseline conditions as well as exhibited the highest CO and CH_4 production rate compared to previous reports. Among the earth-abundant photocatalysts, CuO/P25 had the highest quantum yield for CH_4 (φ_{CH4}: 0.47), whilst CuO/$BaTiO_3$ exhibited highest φ_{CO} (0.09) and stability for CO production. The under-performing of $BaTiO_3$ and CuO/$BaTiO_3$ was attributed to the presence of amorphous phase in $BaTiO_3$. This work reveals that the combination of catalyst design, reaction engineering, and modelling can improve the efficiencies of CO_2 photoreduction.

1. Introduction

CO_2 utilisation for fuels and chemical building blocks plays an important role in detaching societies' reliance on fossil fuels and function within a circular economy [1–4]. Photoreduction of CO_2 offers a promising net zero solution for sustainable energy vector production by directly converting solar energy to fuels [5,6]. However, industrial adoption has been limited due to the low conversion rates and quantum efficiencies. To achieve large-scale application of photocatalytic CO_2 reduction to valuable C_1-products, such as CH_4 and CO, it is essential to develop affordable catalysts coupled with system optimisation and efficient reactor design that promotes high conversion and facilitates variable throughputs.

Titanium dioxide (TiO_2) has been extensively used as a photocatalyst due to its low-cost, abundant availability, and suitable band-position.

However, their large bandgap energy (3.0–3.2 eV), which absorb only UV range, and rapid charge recombination, limit its photocatalytic activity [7,8]. Zinc oxide (ZnO) has also been explored due to its basicity that could enhance CO_2 adsorption. Compared to TiO_2, ZnO (3.3–3.4 eV) suffers from poor charge separation and photo-corrosion [9]. In this context, titanium-based perovskites, such as barium titanate ($BaTiO_3$), have displayed high potential because $BaTiO_3$ (~3.4 eV) exhibits good basicity that aids CO_2 adsorption and activation, and having proper band position for CO_2 photoreduction. Additionally, some crystalline phases of $BaTiO_3$ exhibit ferroelectric properties that further hinders charge recombination, thus, enhancing its photocatalytic activity [10–13]. Although pure $BaTiO_3$ demonstrates satisfactory performance, previous research has shown that modifying the material, such as Ni-$BaTiO_3$ [14] and BiO-$BaTiO_3$ [15], can enhance its catalytic activity and product selectivity.

Co-catalysts, such as metal oxides [16], metals [17], non-noble metals [18], metal sulphides [19], and carbonaceous materials [20], play a crucial role in reducing the reaction potential, supporting interfacial charge transfers, increasing the number of photoactive sites, and improving photon harvesting and reactant adsorption [21]. Among these co-catalysts, copper oxide (CuO) has gained significant attention for CO_2 photoreduction because CuO is non-toxic, abundantly available, displays enhanced absorption of visible light, and possesses excellent CO_2 adsorption capability [22]. Previous studies have demonstrated that CuO impregnated on TiO_2 and ZnO can reduce the charge recombination and achieve efficiencies comparable to noble metal-containing photocatalysts for CO_2 photoreduction [15,23–27]. Unfortunately, thorough study of CuO impregnated $BaTiO_3$ (CuO/$BaTiO_3$) to understand the synergetic effect of CuO and $BaTiO_3$ has not been carried out. Therefore, this study aims to investigate the performance of CuO impregnated $BaTiO_3$ (CuO/$BaTiO_3$) for CO_2 photoreduction and compare it with pristine $BaTiO_3$, and commercial TiO_2 (Evonik P25) and ZnO impregnated with CuO. This exploration of CuO/$BaTiO_3$ as a photocatalyst for CO_2 reduction represents a novel avenue of research in the field, with the potential to uncover new insights and improvements in photocatalytic performance.

In addition to catalyst development, tailoring reaction conditions is also key to accessing the photoactive sites, which can influence the yield and product selectivity, as summarised in Table S1. Due to the lack of standardisation in testing conditions, it is necessary to investigate their role in the perspective of evaluating the process parameters and compare the performance of various photocatalysts within the same operational conditions. Olivo et al [28]. previously investigated the effect of time and irradiance on conversion, concluding that both irradiance and time have a significant impact on CH_4 production under low irradiance conditions. In particular, the concentration/partial pressure of the reactants plays a significant role on the reaction performance and the product yield and selectivity [29]. Thompson et al. discussed that low CO_2 partial pressures favours CO production [30]. In contrast, Dilla et al. reported that increasing the concentration of CO_2 (<1000 ppm) accelerated the formation of CH_4 up to an optimum [31]. Likewise, the concentration of water in the system plays a significant role as an oxidant and a proton donor, which results in a facile transfer from the oxidation to reduction sites [32].

To improve the performance of CO_2 photoreduction systems, a deep learning and understanding of the influence of the CO_2:H_2O along with other process parameters, on the conversion rates and desired product yields is required. Furthermore, there is a critical need for modelling methods to evaluate the fluid dynamics of reactions and display the transport of photons in the reactor whilst considering the reaction kinetics, and mass and heat transfer [33]. Computational fluid dynamic (CFD) models can provide insights into the reactor geometry, fluid flow, mass transfer, photon transport and their influence on the chemistry and physics inside the system [34]. Coupling CFD with Design of Experiments (DOE) can be utilised to investigate the synergetic effects of the reaction and the effect of process parameters on the system that provide insight beyond the experimental limitations without acquiring a large of number of experimenting runs [33,35–40]. Hence, by employing DOE and a first principles-based CFD model, this study investigates the impact of the CO_2:H_2O, irradiance and gas flowrate on the product yield, selectivity, and CO_2 utilisation rate of $BaTiO_3$ and CuO-$BaTiO_3$. Notably, the optimised catalyst loading on our setup has been studied previously [41]. Hence, this parameter is excluded from this study.

2. Materials and methods

2.1. Material Synthesis

2.1.1. Zinc Oxide (ZnO)

ZnO was synthesized by precipitation following Ref [42]. Briefly, 7.11 g of Zn $(NO_3)_2 \cdot 6 H_2O$ (Sigma-Aldrich, ≥99%) was dissolved in

50 mL of milli-Q H_2O. The solution was added dropwise with a peristaltic pump to an aqueous solution adjusted at pH 10 with NaOH 2 M (Sigma-Aldrich, ≥98%) under magnetic stirring. During the addition, the pH was continuously adjusted with NaOH 2 M solution. After the addition, the solution was left under stirring at 500 rpm until it turned opalescent. It was then transferred into a flask and put under reflux with ethylene glycol at 60 °C for 20 h. The solid was rinsed and filtered with sufficient H_2O (until pH 7) and dried in an oven at 110 °C. The material was further treated with calcination in a quartz tube at 600 °C for 2 h.

2.1.2. Copper oxide (CuO)

CuO nanoparticles (NPs) were synthesized following the protocol reported previously [43]. Briefly, 2.0 g of $CuSO_4 \cdot 5 H_2O$ was dissolved in 50 mL of milli-Q H_2O and left under stirring in a beaker covered with a watch glass at 900 rpm for 30 min. NaOH 4 M (Sigma-Aldrich, ≥ 98%) was then added dropwise until pH 8.5 was achieved. The solution was then left under stirring at 1000 rpm for 3 h. Then, the colour of the solution changed from light blue to teal green. The solution was then transferred into a Teflon flask and heated in an autoclave at 180 °C for 18 h. After the hydrothermal treatment, the obtained powder was filtered and washed with sufficient milli-Q water and ethanol. After that, it was left to dry in the oven at 110 °C overnight. The sample was calcinated at 300 °C for 3 h under N_2 atmosphere.

2.1.3. Barium titanate ($BaTiO_3$)

$BaTiO_3$ was synthesized by a solvothermal process, modified from the literature [10]. 50 mL of $BaCl_2$ 0.1 M solution (Fluka Analytical) and titanium (IV) isopropoxide (Sigma-Aldrich, 97%) in equal molar quantity were put in a beaker and the pH was adjusted to 12 with NaOH 4 M (Sigma-Aldrich, ≥ 98%). The solution was left under stirring for 1 h and then put under hydrothermal treatment in an autoclave at 180 °C for 8 h. The sample was filtered and washed with H_2O and ethanol, then dried in an oven at 110 °C overnight.

2.1.4. CuO/$BaTiO_3$, CuO/ZnO, and CuO/P25

TiO_2 was used in its commercial form, *i.e.*, Degussa P25 (Evonik, Italy). To obtain CuO/ZnO, CuO/P25, and CuO/$BaTiO_3$, the support material (*i.e.,* ZnO, P25, or $BaTiO_3$) was impregnated with 2.5 wt% CuO nanoparticles previously synthesized. Briefly, a known amount of CuO was taken and put into a glass vial, dispersed in 1 mL of ethanol, and sonicated for 30 min. The alcoholic solution was added dropwise to the support material, which was put in a crystallizer with the help of a Pasteur. When the powder was wet, it would be moved into the oven to evaporate the excessive solvent. The material was then dried in the oven overnight at 110 °C.

2.2. Material characterisations

The morphology of the synthesized products was examined by a field emission scanning electron microscopy (FE–SEM, Quanta 200 F FEI) equipped with an energy–dispersive X–ray spectroscopy (EDX) detector and a high-resolution transmission electron microscope (HRTEM, FEI Titan Themis 200) operated at 200 kV. Crystallinity and phase identification of the synthesized products were conducted using powder X–ray diffraction XRD (Bruker D8 Advanced Diffractometer) equipped with Cu Kα radiation ($\lambda = 1.5418$ Å) and compared with the ICDD–JCPDS powder diffraction file database. X–ray photoelectron spectrum (XPS) analysis was performed using a Thermo Fisher Scientific NEXSA spectrometer. The samples were analysed using a micro-focused monochromatic Al X-ray source (19.2 W) over an area of approximately 100 μm. Data was recorded at pass energies of 200 eV for survey scans and 50 eV for high resolution scan with 1 eV and 0.1 eV step sizes, respectively. Charge neutralisation of the sample was achieved using a combination of both low energy electrons and argon ions. C 1 s electron at 284.8 eV was used as standard reference to calibrate the photoelectron energy shift. All the data analysis was performed on the XPSPEAK

software (version: 4.1). The chronoamperometric measurement was conducted on the Autolab PGSTAT302N electrochemical workstation with a standard three–electrode system. A Xenon UV lamp (LAX-C100 by Asahi Spectra USA) was used as the light source. To fabricate the working electrode, 20 mg of powder sample were dispersed in 2 mL of ethanol followed by sonication for 1 h. The solution obtained was spin-deposited onto a piece of fluorine doped tin oxide (FTO) glass to coat an area with dimensions 1 cm × 1 cm. Then, the prepared film was air-dried and annealed at 200 °C overnight. Pt wire and Ag/AgCl (KCl 1 M) were used as the counter and reference electrodes, respectively. The electrolyte used was 1 M of KOH aqueous solution.

2.3. CO₂ photoreduction test

CO_2 photoreduction tests were performed to investigate the performance of earth-abundant photocatalysts and optimise the process parameters. The prepared photocatalyst samples were tested for CO_2 photoreduction using the procedures described previously [44]. Briefly, 10 mg of the photocatalyst was dispersed in 1 mL of ultrapure water and sonicated for 5 min. This solution was then deposited with a Pasteur pipette on a glass microfiber filter disk (Whatman GF/C, diameter 47 mm), and dried in the oven at 120 °C for 2 h. The photoreduction experiments were carried out in a thin film fixed bed photoreactor with a simple design that ensures the driving force of the reduction reaction only depends on the solar energy/incident light [45,46]. The photoreactor consisted of a stainless-steel base, in which the glass microfiber filter disk coated with photocatalysts was placed. The photoreactor was then sealed by a stainless-steel lid with a quartz window (diameter 5.5 cm, depth 1.1 cm) [28]. A schematic diagram of the reactor is shown in Fig. 1.

Prior to the photoreduction experiment, the photoreactor was evacuated with a vacuum (−1 bar) and then purged with pure CO_2 (1 bar) [30]. This process was repeated 3 times. Finally, the CO_2 was released through the GC injection port leaving the system at a constant pressure of 0.2 bar throughout the experiment. Thereafter, the flow rate of CO_2 and argon was set according to the experimental conditions ensuring a total gas flow of 0.35 mL min⁻¹ was maintained throughout the experiments. The gas mixture was purged through a temperature-controlled saturator filled with milli-Q water overnight to allow the system to reach equilibrium. The humidity in the system was continuously monitored and recorded using an inline Sensirion SHT75 humidity sensor placed (MG Chemicals 832HD) connecting to a Swagelok 1/4" T-piece. The temperature of the photoreactor was maintained and controlled using a hotplate (at 50 °C) and the temperature of the gas line was heated using a heating cord and thermocouple. The temperature of the photocatalyst inside the reactor was measured using an IR thermometer (Stanley STHT77365 s1mW, 630–660 nm).

LAX-C100 Asahi Spectra light source with a wavelength between 240 and 1000 nm and a collimator lens (model KLQφ5 Asahi Spectra) was placed 12.5 cm above the surface of the glass fibre disk. The irradiance was measured using a One Sun Checker (Asahi Spectra CS-20) and the intensity was adjusted to meet the required irradiance (Table S2). A dark

reaction was performed prior to the light being switched on; no product was observed.

An inline GC (Agilent, Model 7890B series) with a Hayesep Q column (1.5 m), 1/16 in. od, 1 mm id), MolSieve 13X (1.2 m), 1/16 in. od, 1 mm id), thermal conductivity detector (TCD), nickel catalyzed methanizer for the detection CO and CO_2 and flame ionization detector (FID) was used to analyse the output of the photoreaction. The data output from the GC was used to calculate the cumulative production of CO, CH_4, O_2, H_2, N_2, and CO_2 by integrating the area using MATLAB [28,42,44].

Cyclability tests of the $CuO/BaTiO_3$ photocatalyst were done with three cycles of 3-h reactions. Between the cycles, the photocatalyst (*i.e.*, $CuO/BaTiO_3$) loaded on the glass microfiber disk was regenerated by placing it in the oven at 120 °C for 2 h to remove absorbed molecules such as water. The catalyst disk was placed back into the reactor, sealed, and was prepared for the next cycles following the experimental procedures mentioned above. XRD analysis of the sample was performed. In particular, the analysis was conducted for the bare glass microfiber disk with and without a thermal treatment in the oven at 120 °C for 2 h, $CuO/BaTiO_3$ loaded onto the support both air-dried and dried in the oven – the latter considered the 'pre-reaction' stage – and for the catalyst after one and three cycles of reaction.

The performance of the system was evaluated using the cumulative production of the products, the quantum yield, and the CO_2 utilisation rate. The quantum yield (φ) in photocatalysis measures the rate between the amount of product produced and the number of photons absorbed by the photocatalyst at a specified wavelength (λ)[28]. φ values for CO, CH_4 and H_2 evolution for CO_2 photoreduction were calculated according to Eq. (1). The incident flux was determined by a BLACK-Comet F600-UV-SR Spectrometer (StellarNet Inc.) when the photocatalyst was irradiated under the UV light lamp (LAX-C100 Asahi Spectra). The CO_2 utilisation rate was calculated by taking the mole% of CO_2 inlet: CO_2 outlet as the amount of CO_2 consumed [22].

$$\varphi_{product}(\lambda) = \frac{\text{amount of product formed}}{\text{amount of photons absorbed}(240 - 400 \text{ nm})} \tag{1}$$

2.4. Design of experiments

To assess the impact of reaction conditions on the desired product selectivity and identify optimal reaction conditions, a systematic approach utilising Design of Experiments (DOE) was employed. The primary focus of employing DOE was to mainly investigate the effect of irradiance and the CO_2:H_2O on the product yield and selectivity.

The CO_2:H_2O was experimentally varied by utilising a mass flow controller to regulate the CO_2 gas flow, while adjustments in the H_2O concentration was accomplished by varying the temperature of the bubbler in the saturator. Consequently, the variables under investigation in this study consisted of irradiance, flow rate of CO_2, and flow rate of H_2O (controlled *via* the bubbler temperature). The design of experiments was set up using a two-level full factorial design with 3 factors and 3 centre points, building up to 11 experimental runs. The experimental ranges for the variables are highlighted in Table 1. It is important to note that these ranges were selected with due consideration for constraints imposed by the reactor setup. For instance, the upper limit of the irradiance was determined by the detection capability of the sun checked, *i.e.*, the highest measurement was 125 mWcm⁻². Additionally, the
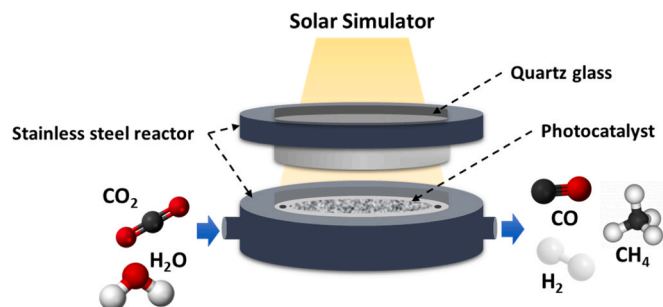
Fig. 1. Schematic of the photoreactor.

Table 1
Experimental variables for CO_2 photoreduction.

Variable	Low (−1)	Medium (0)	High (+1)
Irradiance (mWcm⁻²)	75	100	125
CO_2 Flow (mL min⁻¹)	0.09	0.22	0.35
H_2O Temperature (Bubbler temperature, °C)	25	30	35

maximum gas flow rate into the reactor is restricted to 0.35 mL min^{-1} and the maximum temperature of the bubbler was limited to 35 °C to prevent system flooding. Each experiment was conducted for 4 hr using the $CuO/BaTiO_3$ catalyst. Using the cumulative production results for the products CO, CH_4 and H_2, the results were analysed using Minitab software with a confidence level of 0.95.

2.5. Simulation study

2.5.1. Model Development

This simulation study builds a rigorous model of the photoreactor while integrating the fluid dynamics, reaction kinetics, and radiation field. Proposed by Oliveira De Brito et al [33]. three steps are required to develop a CFD model of the photoreactor: the hydrodynamic model, the radiation model, and the kinetic model as illustrated in Fig. 2 [33]. The hydrodynamic model defines the flow characteristics and species transport, whilst the objective of the kinetic and radiation models are to determine the rate of the CO_2 photoreduction reaction considering light intensity [33].

Using COMSOL V6.0 software, a stationary three-dimensional model of the photoreactor was developed and compared against the experimental data obtained from this study. The inlet gas in the model was set as a mixture of Ar, CO_2, and H_2O (vapour). Detailed information about the model parameters are listed in Table 2. The model was built with the gas flow in the steady state with the following assumptions applied:

1. The fluid flow is in the laminar regime (*i.e.,* $Re_{in} < 0.1$) as the average flow field is proportional to the pressure difference across the reactor.
2. No slip is the default boundary condition for a stationary solid wall for laminar flow.
3. The gas in the reactor is assumed to be ideal with constant physical properties.
4. The gas mixture enters the reactor at the inlet with a uniform constant velocity distribution.
5. The reactor wall is adiabatic and the temperature distribution across the reactor is uniform.
6. The heating caused by the UV lighting is negligible which was experimentally justified.
7. The steady-state model only considers the reaction profile when the photocatalysts are active.

2.5.2. Hydrodynamics model

The gaseous fluid flow (CO_2, Ar and H_2O vapour) in the photoreactor occurs at atmospheric pressure and temperature. Hence, the gas can be considered a Newtonian incompressible fluid with constant physical

Table 2
Model parameters.

Type	Variable		Value	Unit
Geometry	R_h	Reactor Height	1	mm
	R_d	Reactor Diameter	50	mm
	S_d	Catalyst Support Diameter	47	mm
	S_t	Catalyst Support Thickness	0.2	mm
	d_{in}	Gas inlet Diameter	0.6	mm
	d_{out}	Gas outlet Diameter	0.4	mm
Conditions	T	Temperature	36	°C
	P	Pressure	101	kPa
	V	Inlet Gas Flow Rate	0.35	mL/min

properties [47]. Moreover, for a single-phase gaseous fluid flow system the mass balance can be described using total mass conservation and the momentum balance using the Navier-Stokes equation [33,48]. Therefore, the following equations were used to solve the mass balance of the reacting species in the photoreactor:

- The continuity equation that represents the conservation of mass:

$$\nabla \rho \bullet u = 0 \tag{2}$$

- The momentum equation uses Navier-Stokes equation to represent the conservation of momentum for an incompressible flow:

$$\rho(u \bullet \nabla u) = \nabla \bullet \left[-\rho + \mu \left(\nabla u + (\nabla u)^T \right) \right] + F \tag{3}$$

- The mass transport of the chemical species governed using Fick's Law:

$$\nabla \bullet (-D_i \nabla c_i) + u \bullet \nabla c_i = R_i \tag{4}$$

where ρ is density (kg/m^3); u is velocity (m/s); μ is viscosity (m^2/s); T absolute temperature (K); F is the volume force vector (N/m^3); D_i diffusivity of species i (m^2/s); c_i molar concentration of species i (mol/m^3); R_i is the reaction rate expression for the species (mol/m^{3}s).

The conservation of mass and continuity equations were solved by the laminar flow module using the default P1 (velocity) + P1 (pressure) discretization. Whilst the mass transport of the chemical species was solved using the transport of diluted species module which provides a modelling environment for the evolution of chemical species transported by diffusion and convection. This physics interface assumes that all species present in the system are dilute. For this module, the concentration of the species was discretised using the linear method.
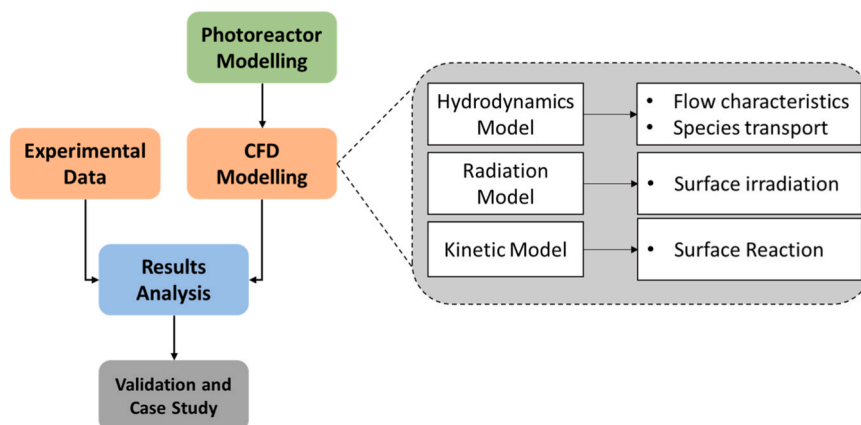

Fig. 2. CFD simulation flowchart.
Adapted with permission from Ref [33].

2.5.3. Reaction kinetics and radiation model

The reaction kinetics identifies the pathway and rates of the reactions taking place within the system. Numerous reaction mechanisms have been proposed for CO_2 photoreduction processes with the three dominant pathways being the formaldehyde, carbene and glyoxal pathways. The reaction mechanisms that has been widely reported for CuO-based and TiO_2-based photocatalyst are the formaldehyde and carbene pathways [22,23,49]. Using $BaTiO_3$ based catalyst the dominant reaction pathway reported is $CO_2 \rightarrow CO \rightarrow COH \rightarrow HCHO \rightarrow CH \rightarrow CH_2 \rightarrow CH_3 \rightarrow CH_4$ with the hydrogenation of CO being the rate determining step mirroring the carbene pathway [14]. Therefore, to carry out this simulation it was necessary to simplify the representation of the reaction intermediates, focusing on the direct production of CH_4 and CO from CO_2. Hence, this simulation incorporates the following pseudo-first-order surface reactions:[50,51].

$$2H_2O = 2H_2 + O_2 \tag{5}$$

$$CO_2 + H_2 = CO + H_2O \tag{6}$$

$$CO_2 + 2H_2O = CH_4 + 2O_2 \tag{7}$$

For heterogeneous photocatalytic reactors, several studies have related the kinetics closely to surface adsorption [18,37,48,52–54]. This association stems from the fact that the reaction kinetics highly depends on the catalyst surface reactions. Consequently, due to the dearth of a more comprehensive alternative, the Langmuir-Hinshelwood (LH) or derived variations have been widely adopted to describe the kinetics of CO_2 photoreduction. The LH derived kinetic model assumes that the rate of the reaction varies linearly with the light intensity at every point in the reactor:[53].

$$r = k_r I^\alpha \frac{\prod_{i=1}^{n} K_i C_i}{\left(1 + \sum_{i=1}^{z} K_i C_i\right)^n} \tag{8}$$

where r is the rate of reaction (μmol gcat^{-1} h^{-1}); k is the rate constant (μmol gcat^{-1} h^{-1}); I is the irradiance; α is the reaction order of light intensity; K is the equilibrium adsorption constant for reactants (m^3/mol); C is the concentration of reactant(s) (mol/m^3); n is the adsorbed reactants involved in the elementary surface reaction; z is the total reactants and products. At low concentrations the factors $KC < <1$, therefore the equation is reduced to:[52].

$$rate, r = k_t I^\alpha C_{reactant(s)} \tag{9}$$

$$k_t = k_r K \tag{10}$$

The rate constant for the photoreduction reaction can vary depending on numerous factors such as the quantum yield, light intensity and absorptivity, concentration of active sites on catalyst, and the extinction coefficient [55]. Therefore, the rate constant used in this model is the apparent activation rate constant k_t derived from the experimental data.

The distribution of the light intensity plays a crucial role in assessing the performance of the system. To model the light distribution in photocatalytic systems, the radiation transport equation (RTE) is widely adopted. The RTE describes the transmission of the photons from the light source, accounting for their respective energies and incorporating any losses resulting from absorption and/or scattering processes [33]. In the system under focus, the catalyst is immobilised, and the reaction occurs on the surface of the catalyst (excluding considering of porous zones). Quantification of the scattering and absorption of light in this system is challenging, thus the RTE reduces to the Beer-Lambert Law [33,48].

$$I = I_0 e^{-\mu_L z} \tag{11}$$

where I_0 is the incident light intensity; μ_L is the attenuation coefficient; z is the depth of the light travelling through the surface.

3. Results and discussion

3.1. Catalyst characterization

3.1.1. Crystal phase

The crystal phases and crystallinity of the synthesized samples were characterized using XRD (Fig. 3). The synthesized $BaTiO_3$ before and after impregnating with CuO (*i.e.*, CuO/BaTiO$_3$, Fig. 3a and b) exhibited the tetragonal perovskite structure with the most intense peak (110) at $2\theta = 32.2°$. Additionally, other weak peaks centred at $2\theta = 22.2°$ (110), $38.9°$ (111), $45.6°$ (200), $56.1°$ (211), $65.8°$ (220) were observed (JCPDS No. 31–0174), confirming the formation of perovskite [56]. The broad peak at small Bragg angles indicated the presence of amorphous part of the sample. Pristine ZnO and CuO-impregnated ZnO (*i.e.*, CuO/ZnO) presented the peak pattern of a hexagonal cell (JCPDS No. 36–1451), in which the most intense peak is centred at $2\theta = 36.2°$ (101) and minor peaks appear at $2\theta = 36.7°$ (100), $34.4°$ (002), $47.6°$ (102), $56.6°$ (110). Pristine and impregnated P25 (*i.e.*, CuO/P25) exhibited the characteristic peaks for anatase (JCPDS No. 21–1272) at $2\theta = 25.2°$ (101), 37.8 (004), $48.0°$ (200), $53.9°$ (105), $55.0°$ (211), $62.6°$ (204) and rutile (JCPDS No. 21–1276) at $2\theta = 27.4°$ (110) $36.1°$ (101), $41.2°$ (111), $54.7°$ (211), $62.9°$ (103), $67.9°$ (112). In the impregnated samples, no significant changes in the position of peaks upon impregnation with CuO was observed, indicating the formation of monoclinic structured CuO and ruling out alloying of CuO with TiO_2 [27].

3.1.2. Morphology

The morphology of the synthesized materials was analysed by SEM-EDX and HRTEM. $BaTiO_3$ and CuO/BaTiO$_3$ samples showed a combination of agglomeration and fibre-like structure (Fig. 4a and b). The elemental distribution (*i.e.*, Ba, Ti, and O) of the synthesized $BaTiO_3$ and Cu of the CuO/BaTiO$_3$ (Fig. 4b) was evenly distributed. The fabricated CuO/P25 showed dispersive nanoparticles without severe agglomeration after impregnating with CuO (Fig. 4c), meanwhile, the synthesized CuO/ZnO exhibited dispersive rice-grain microstructure (Fig. 4d). The impregnation of CuO was successfully imbued onto ZnO and P25 (Fig. 4c and d, respectively). The faint EDX signal of Cu K was attributed to the low concentration (2.5 wt% as nominal percentage in every impregnated sample).

The HRTEM revealed that $BaTiO_3$ presented polycrystalline and amorphous structures (Fig. 5a and b). As for CuO/BaTiO$_3$, the CuO cluster was observed, accumulating on the surface of $BaTiO_3$ (Fig. 5c). The diffraction pattern of CuO was observed well-defined (Fig. 5d),
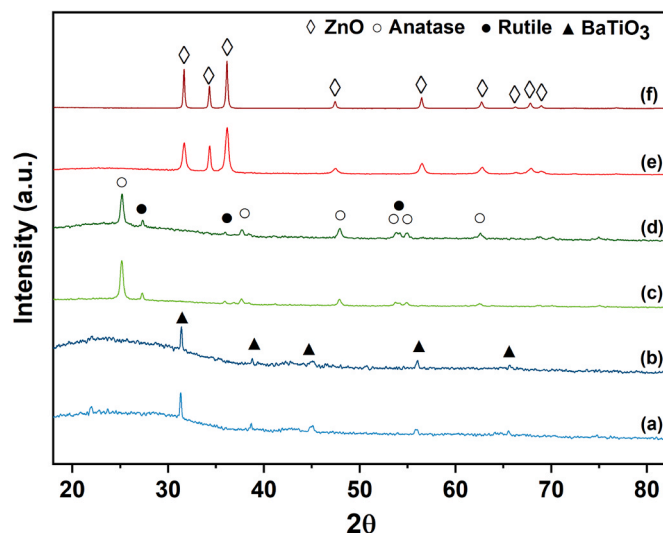

Fig. 3. XRD spectra of (a) BaTiO$_3$, (b) CuO/BaTiO$_3$, (c) P25, (d) CuO/P25, (e) ZnO and (f) CuO/ZnO.
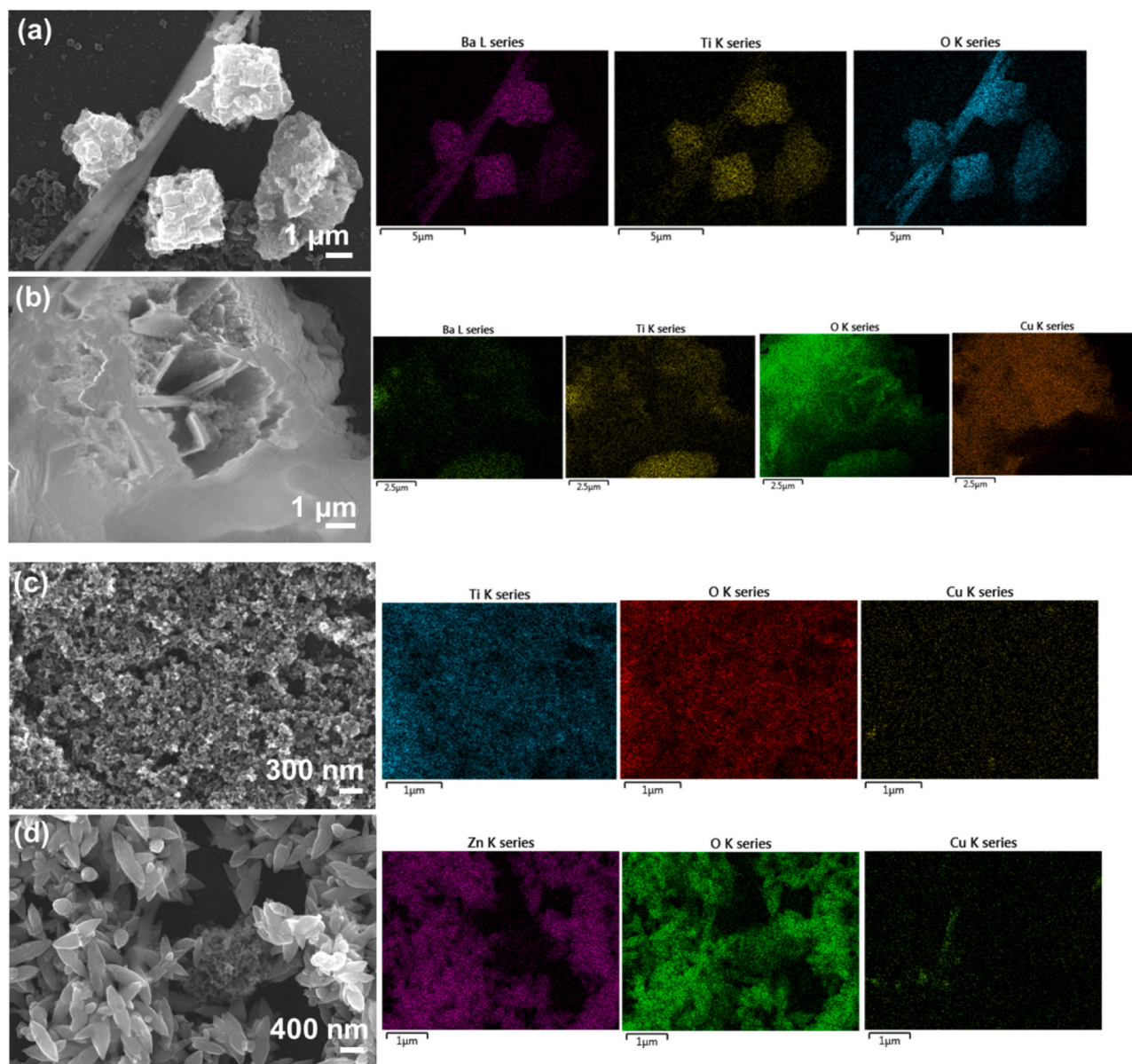
Fig. 4. SEM-EDX images of (a) BaTiO$_3$, (b) CuO/BaTiO$_3$, (c) CuO/P25, (d) CuO/ZnO.

confirming highly crystalline phase of CuO in the absence of pronounced amorphous background [57].

3.1.3. Electronic properties

The estimated bandgap energy of BaTiO$_3$, CuO/BaTiO$_3$, CuO/P25 and CuO/ZnO using diffused reflectance was 3.5, 3.3, 2.8 and 3.0 eV, respectively (Fig. S1). The photon-to-current properties of the samples were elucidated using chronoamperometry results (Fig. S2). Each sample showed rapid response to the light source (*i.e.*, UV light), manifesting the excitation of electrons by light radiation, with response magnitudes varying among the samples. Having the largest bandgap energy among the samples, sample BaTiO$_3$ exhibited the lowest photon-to-current density. After the impregnation of CuO into BaTiO$_3$, CuO/BaTiO$_3$ sample showed four times higher in the current density compared to the pristine BaTiO$_3$. Conversely, CuO loading did not have a significant effect on P25. The CuO/ZnO sample showed the greatest current density among the samples; nevertheless, it also showed significant decay over time due to light corrosion.

3.1.4. Surface chemistry

X-ray photon spectroscopy (XPS) was performed to gain information on the stoichiometry, superficial species of the sample and the surface chemistry. The Ba 3d orbitals of BaTiO$_3$ and CuO/BaTiO$_3$ (Fig. S3) were centred at 779.1 and 794.6 eV, attributing the 3d$_{5/2}$ and 3d$_{3/2}$, respectively. The calculated value of the spin-orbit splitting (15.5 eV) is in accordance with the presence of Ba^{2+} attested in literature [58]. In addition, Ti 2p was positioned at 457.9 (2p$_{3/2}$) and 463.9 eV (2p$_{1/2}$) with a splitting distance of 6.0 eV, confirming the presence of Ti^{4+} in the lattice [59]. O 1 s peak was located at 529.4 eV, evidencing the Ba-O-Ti bond [60]. Minor peaks at 530.5 and 531.5 eV were attributed to Ti-O-Ti bonds and adsorbed oxygenated species, respectively [60,61].

The relative atomic% of each element is tabulated in Table 3. The Ba: Ti ratio of BaTiO$_3$ and CuO/BaTiO$_3$ samples exhibited a much higher ratio compared to the stoichiometry of the compound (*i.e.*, Ba:Ti 1:1). The excess of Ba might be beneficial to CO$_2$ adsorption [62]. CuO/BaTiO$_3$ shows a higher presence of oxygen, which is in accordance with the Ti/O ratio of 1:3. The ratio is not respected in the pure perovskite, with a value of 1:1.4. This leads to a greater exposure of superficial Ba and could support the tendency of the material to form carbonates [62]. The
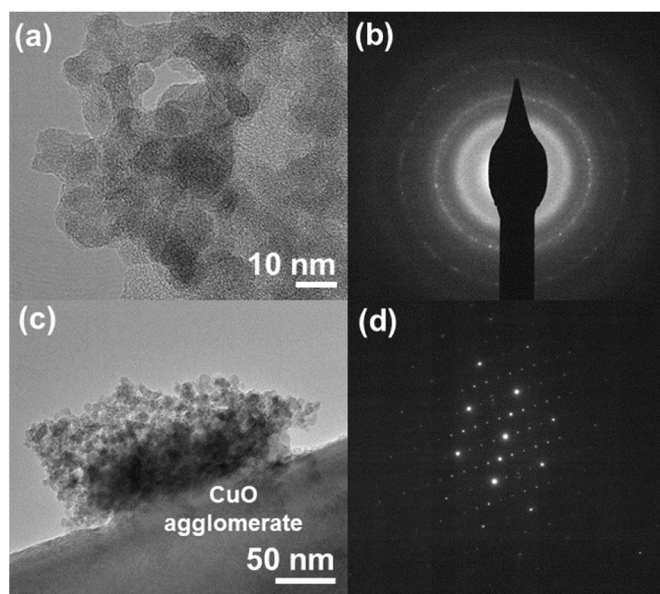
Fig. 5. (a) HRTEM image and (b) diffraction pattern of $BaTiO_3$; (c) HRTEM image of $CuO/BaTiO_3$ and SAED was acquired on the CuO cluster.

Table 3
Relative concentration of element (atomic%) of the synthesized samples.

Sample	% Ba	% Ti	% Zn	% O	% Cu	% C
$BaTiO_3$	54	17	-	24	-	5
$CuO/BaTiO_3$	42	13	-	38	5	2
P25	-	45	-	46	-	9
CuO/P25	-	41	-	37	13	9
CuO/ZnO	-	-	80	11	7	2

presence of Cu is attested at 5% with respect to the surface from the integration of the detected peaks.

As for P25 and CuO/P25 (Fig. S4 a and b), Ti^{4+} 2p characteristic peaks could be detected for both samples at 458.8 and 464.6 eV, for $2p_{3/2}$ and $2p_{1/2}$, respectively, with a spin-orbit splitting value of 5.8 eV. O^{2-} 1 s peaks were detected at 529.6 eV. Weak peaks at 530.8 and 531.8 eV could be related to adsorbed species [63]. Relative atomic% were slightly different, but the Ti/O ratio was close to 1:1 for both specimens, highlighting the presence of superficial oxygen vacancies. Carbon was present with a percentage ~9%, advancing the possibility of the presence of superficial carbonaceous species. The Cu atomic% for CuO/P25 observed was higher than $CuO/BaTiO_3$ probably due to the highly dispersive CuO. As for CuO/ZnO spectra (Fig. S4c), Zn 2p orbitals were detected at 1021.3 and 1044.2 eV for $2p_{3/2}$ and $2p_{1/2}$, respectively, having 22.9 eV confirmed the formation of Zn^{2+} in the wurtzite ZnO

structure [24]. The O 1 s peak centred at 530.3 eV was representative of the Zn-O bond, whereas the shoulder peak centred at 531.7 eV was deemed related to superficial hydroxyl species [64]. Nevertheless, the intensity of the Zn peaks compared to O showed a major percentage of oxygen vacancies within the sample. The relative concentration of Cu within CuO/ZnO was estimated to be 7%.

3.2. Optimisation of CO_2 photocatalytic reduction

3.2.1. Design of experiments

The experimental outputs of the DOE (Table 4) was analysed using Minitab software to elucidate the influence of each parameter on the production of CO, CH_4 and H_2. Pareto charts and main effects plots (Fig. 6, S5 and S6) were utilized for data visualisation and inference. Pareto charts provide insight into the magnitude of each operating condition's impact on the cumulative production of the products. With a confidence level of 95%, the Pareto charts indicate the statistical significance of each parameter (*i.e.*, *p*-value $< \alpha = 0.05$) [65].

Pareto charts revealed that the presence of H_2O in the system exhibited significant influence on the cumulative CO production (p value = 0.001, Fig. 6a), followed by irradiance and CO_2 flow (p value = 0.005 and 0.02). The main effects plots (Fig. S5) revealed that increasing the H_2O (bubbler) temperature and irradiance lead to an increase in the mean of CO production, whereas higher CO production is observed at low CO_2 flowrates. Equation 15 represents the model for the statistically significant terms. Conversely, the individual parameters did not demonstrate any statistical significance for CH_4 and H_2 production (Fig. 6b and c). Further analysis (Fig. S6) highlighted that CH_4 production was significantly affected by the combination of CO_2 flow and H_2O temperature, as well as their interaction with irradiance (*p* values = 0.001).

Cumulative production of CO (μmol g_{cat}^{-1}) = −138.5 to 122.3 CO_2 Flow (mL min^{-1}) + 5.91 H_2O Temperature (°C) + 0.869 Irradiance (mWcm^{-2}) - 39.32 *(15)*.

When the irradiance in this study increased from 75 to 175 mW cm^{-2}, the overall cumulative CO production was increased and the highest CO production (119.6 μmol g^{-1}) was achieved when the CO_2:H_2O was 9 under 125 mW cm^{-2} of irradiance, 0.09 mL min^{-1} of CO_2 flow at 25 °C of bubbler temperature. However, the CH_4 production showed a different trend compared to that of H_2 and CO production when the irradiance increased to 125 mW cm^{-2} (Fig. 7a). A better product selectivity was observed when the CO_2:H_2O achieved 30 (301.5 μmol g^{-1} with 0.35 mL min^{-1} of CO_2 and 35 °C of bubbler temperature). Although the overall yield obtained under the high value parameters (125 mW cm^{-2} of irradiance, 0.35 mL min^{-1} CO_2 flow and 35 °C bubbler temperature, Table 4), the practical operation challenges encountered, including the control of high (>30 °C) bubbler temperature, lead to system flooding. As a result, the parameters that yielded higher CO were selected as the optimised parameters (*i.e.*, 125 mW cm^{-2}, CO_2 flow: 0.09 mL min^{-1}, bubbler temperature: 25 °C). Notably, compared to the baseline conditions (*i.e.*, 100 mW cm^{-2}, CO_2
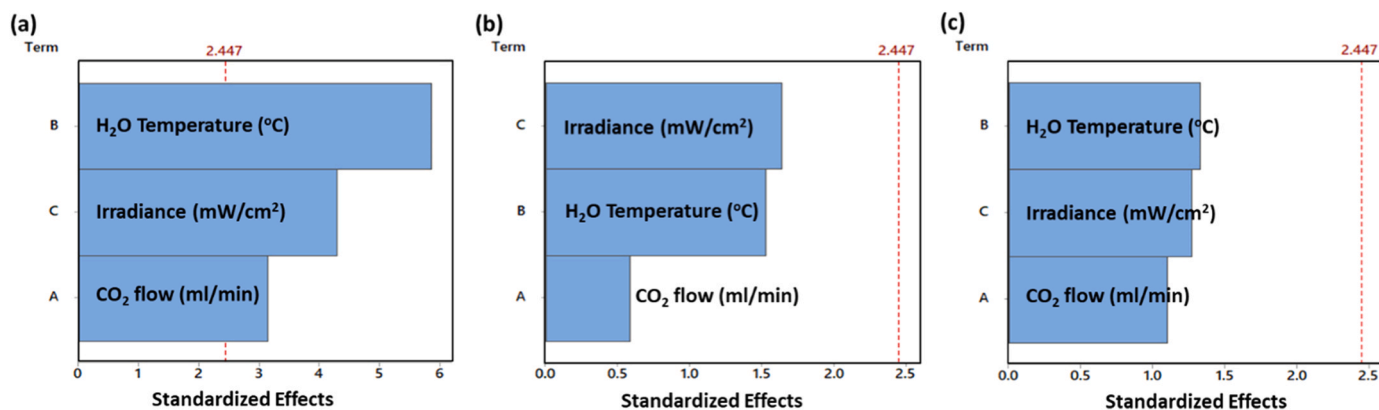
Table 4
Details of the experimental design parameters and cumulative production (4 h) of products from CO_2 photoreduction reduction using $CuO/BaTiO_3$ photocatalyst.

Irradiance (mWcm^{-2})	CO_2 Flow (mLmin^{-1})	H_2O Temperature (Bubbler T °C)	CO_2/H_2O	CO Cumulative Production (μmol g^{-1})	CH_4 Cumulative Production (μmol g^{-1})	H_2 Cumulative Production (μmol g^{-1})
75	0.09	25	Low (9.6)	46.3	11.4	1.7
75	0.35	25	High (38.9)	38.9	16.6	1.9
75	0.09	35	Low (6.8)	119.9	92.4	5.2
75	0.35	35	High (30.1)	103.6	99.0	3.1
125	**0.09**	**25**	**Low (9.5)**	**119.6**	**164.0**	**5.4**
125	0.35	25	High (39.3)	72.5	39.1	1.1
125	0.09	35	Low (8.0)	173.4	64.5	4.6
125	**0.35**	**35**	**High (30.5)**	**117.0**	**301.5**	**75.9**
100	0.22	30	Medium (20.2)	64.1	10.6	3.2
100	0.22	30	Medium (19.4)	48.6	18.1	3.0
100	0.22	30	Medium (19.1)	66.1	18.0	3.6

Fig. 6. Pareto charts of the operating conditions *vs* cumulative production of (a) CO, (b) CH_4 and (c) H_2.
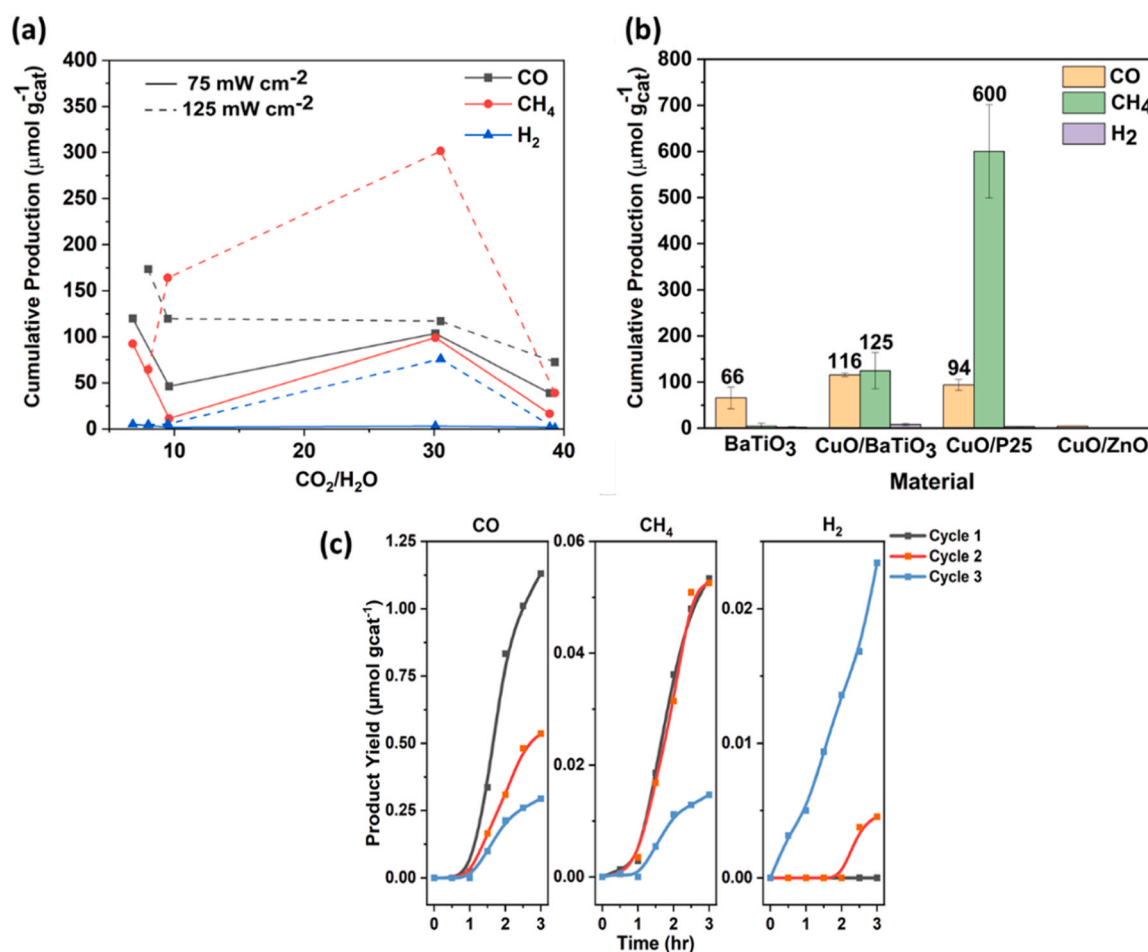

Fig. 7. (a) CO_2/H_2O ratio against cumulative production for CO, CH_4 and H_2 when 75 (solid line) or 125 mW cm^{-2} (dash line) of light source was applied. (b) Cumulative products obtained from different photocatalysts under the optimised conditions (125 mW cm^{-2}, 0.09 mL min^{-1} of CO_2 flow and 25 °C bubbler temperature). (c) CuO/BaTiO$_3$ catalyst cyclability test.

flow: 0.22 mL min^{-1}, bubbler temperature: 30 °C), the CO and CH_4 productions under the optimized conditions were increased by 2 and 10-folds, respectively.

3.2.2. Evaluation of photocatalysts

The performance of the fabricated photocatalyst, namely BaTiO$_3$, CuO/BaTiO$_3$, CuO/P25 and CuO/ZnO, under the optimised reaction conditions were revealed (Fig. 7b). Overall, all the 4 samples showed insignificant production of H_2. Among the samples, CuO/P25 showed

the highest production of CH_4 (*i.e.*, 600 μmol g$_{catalyst}^{-1}$), followed by CuO/BaTiO$_3$ (*i.e.*, 125 μmol g$_{catalyst}^{-1}$), which exhibited the highest CH_4 and CO production in the literature (Table S1); whereas BaTiO$_3$ and CuO/ZnO produced trace amount of CH_4. CuO/BaTiO$_3$ exhibited the highest production of CO (*i.e.*, 116 μmol g$_{catalyst}^{-1}$), followed by CuO/P25 (*i.e.*, 94 μmol g$_{catalyst}^{-1}$) and BaTiO$_3$ (*i.e.*, 66 μmol g$_{catalyst}^{-1}$). CuO/BaTiO$_3$ showed a higher product selectivity towards CO, whereas CuO/P25 showed higher tendency to produce CH_4 although they are tested under similar conditions. A recent study revealed that the concentration of

photogenerated carriers available for the CO_2 activation and subsequent reduction, and water oxidation played a crucial role in determining product selectivity [13]. Hence, it is postulated that the CuO/P25, which showed homogeneous CuO dispersion as shown in Fig. 4c, could provide sufficient photogenerated carriers for CH_4 formation. Meanwhile, the clustered-CuO observed on CuO/BaTiO$_3$ sample showed less efficient photogenerated carriers compared to CuO/P25, leading to higher CO formation. Notably, the CO production rate of CuO/BaTiO$_3$ remained constant after the extended period up to 8 h; whereas CuO/P25 revealed a significant decay in the production after 4 h (Fig. S7).

The quantum yields (φ_{CO} and φ_{CH4} from 240 to 400 nm) of the fabricated sample, which are active mainly in the UV region (Fig. S1), were summarised in Table S3. The φ_{CO} and φ_{CH4} of CuO/BaTiO$_3$ (0.093 and 0.100, respectively) were higher compared to pristine BaTiO$_3$ (0.035 and 0.002, respectively). This result indicated that the incorporation of CuO as a co-catalyst effectively enhances the overall photoactivity of the system, leading to increased CO and CH_4 production. However, the overall production from CuO/BaTiO$_3$ was inferior compared to CuO/P25 (φ_{CH4} of 0.472) probably due to the presence of amorphous phase in BaTiO$_3$. Furthermore, the substantial increase in φ_{CH4} further supports the notion that the co-catalyst CuO has a pronounced effect on enhancing the selectivity towards CH_4. The enhanced performance of CuO/P25 was unexpected according to the chronoamperometry (Fig. S2) and surface area analysis (Table S4), in which CuO/BaTiO$_3$ exhibited higher photo-to-current and surface area as compared to CuO/P25. Hence, we postulated that the superior CO_2 photoreduction performance was attributed to the more evenly distribution of Cu on P25 surface as evidenced in the EDX mapping (Fig. 4c) and XPS analysis (Table 4) that could have taken part into an enhanced photoactivity of CuO/P25 with respect to CuO/BaTiO$_3$. Furthermore, the φ_{CH4} of CuO impregnated P25 exhibited much higher than pristine

P25 (*i.e.*, 0.026) [66] that were tested under similar conditions.

3.2.3. Cyclability tests

Cyclability tests were conducted on CuO/BaTiO$_3$ photocatalyst in three cycles under the optimised reaction conditions for 3 h (Fig. 7c). Throughout the cycles, the CO production exhibited a gradual decrease, indicating a decline in the desired catalytic activity. In contrast, CH_4 production remained relatively constant during the first two cycles. Interestingly, H_2 production slightly increased in the third cycle, which is attributed to the progressive occupation of H_2O molecules on the catalyst surface supporting the hydrogen evolution competitive reaction. Additionally, a noticeable colour change from grey to purple of the photocatalyst was observed, suggesting the reduction of Cu^{2+} to Cu^+. To investigate possible alterations in the photocatalyst, XRD of the sample before and after the reaction was performed (Fig. S8). A weak intensity peak indexed to $BaCO_3$ was observed in the pre-reaction and post-reaction samples after deposition onto the glass microfibre disk. This contamination was deemed due to the high Ba content within CuO/BaTiO$_3$ as evidenced in XPS (Fig. S3) which increased the tendency of the material to form $BaCO_3$ upon exposure to the thermal treatment prior CO_2 photoreduction testing. The formation of $BaCO_3$ could possibly be detrimental to the CO_2 photoreduction capability, thus, the yield obtained from CuO/BaTiO$_3$ was lower than CuO/P25.

3.3. Simulation

A steady-state simulation of the reactor was performed to model the photocatalyst activation period ($1.2 - 4 \pm 0.5$ h) under the optimised reaction conditions. Applying ideal gas laws, a CO_2 flow of 0.09 mL min^{-1} results in a CO_2 partial pressure was 25.17 kPa, whilst at a H_2O temperature of 25 °C corresponded to a H_2O partial pressure of
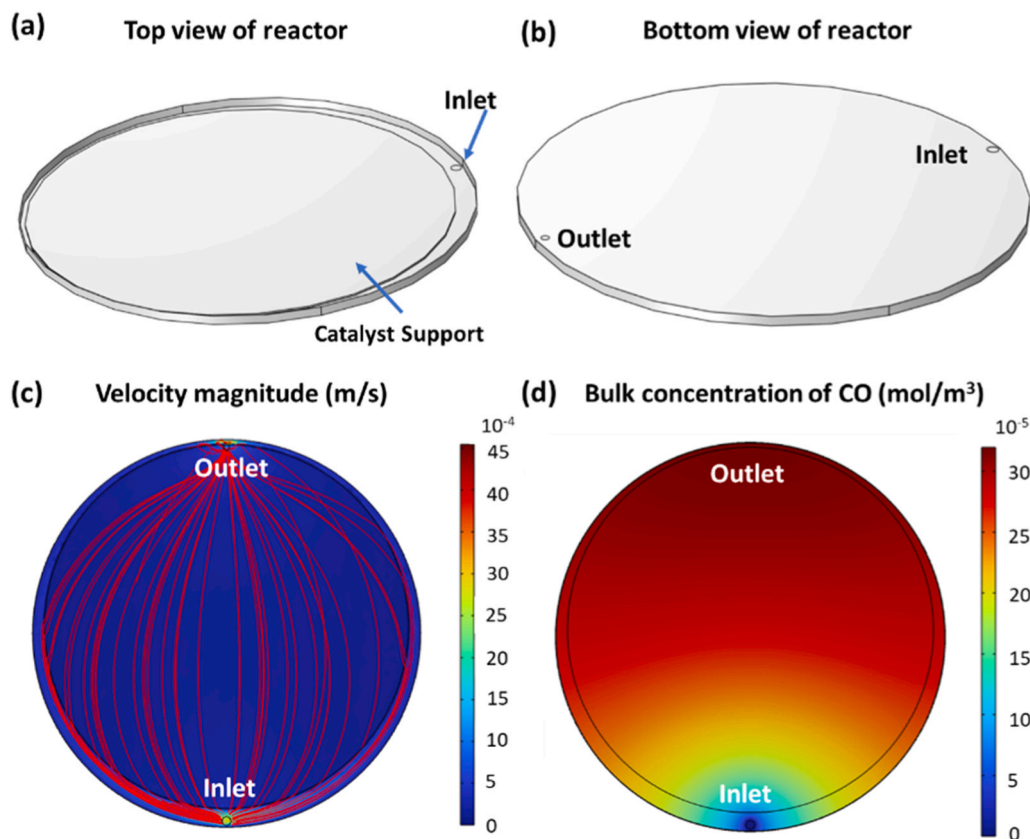

Fig. 8. The (a) top and (b) bottom views of the reactor showing the locations of the photocatalyst, gas inlet and outlet. 2D plots of (c) the gas velocity distribution profile and (d) the bulk concentration of CO during the reaction (using CuO/BaTiO$_3$ photocatalyst).

3.1 kPa. The apparent rate constants for the pseudo-first-order reactions (5) - (7) are presented in Table S5. The simulation model accurately depicted the reactor dimensions under operation (Fig. 8a and b), ensuring the glass fibre disk was positioned above the outlet to increase the residence time and promote inlet gas distribution across the photocatalyst surface. The simulation demonstrates a homogenous gas distribution with gas velocities ranging between 1 and 45×10^{-4} ms^{-1} within the reactor (Fig. 8c). The bulk concentration of CO increased along the direction of flow (Fig. 8d), indicating effective mass transfer in the thin-film reactor design.

Parametric sweep simulations were conducted on all the samples to access the impact of irradiance, total gas flowrate, and H_2O and CO_2 partial pressures beyond experimental limitations, on the CO_2 utilisation rate (Fig. 9). The simulation results closely matched the experimental data under the optimised reaction conditions with a confidence level of $15.00 \pm 5.00\%$. Among the samples, CuO/P25 exhibited the highest product yield and CO_2 utilisation rate. A linear relationship was observed between the CO_2 utilisation rate and the irradiance on the reaction surface, in line with the Beer-Lambert law, which states that the product concentration has a linear relationship with photon absorbance. Conversely, increasing the total gas flowrate resulted in an asymptotic decrease in utilisation rate due to the reduced contact time between the catalyst and reactants.

Increasing the partial pressure of CO_2 initally resulted in a rise in utilisation rate until a pressure of approximately 25 kPa, beyond which most active sites were occupied, leading to a plateau. This phenomenon was witnessed in the DOE experiments, in which an increase in the CO_2/H_2O ratio (from 8.1 to 31.7) significantly increased CH_4 production under high irradiance conditions (125 mW cm^{-2}). On the other hand,

raising the partial pressure of H_2O decreases the utilisation rate due to increased competition of the active sites between the H_2 evolution and CO_2 reduction reactions [30]. The simulation model indicates that having no H_2O in the reactor resulted in higher utilisation rates, but Dilla et al. demonstrated that the product formation decayed with time without the presense of H_2O [67]. This is because water is essential in CO_2 photoreduction as it influences the surface reactions involving H$^+$ or H_2 and stabilises the electron-hole recombination [68,69]. Thus, maintaining a balanced concentration of H_2O in the reactor is necessary to minimise competition between CO_2 and H_2O for the photogenerated holes.

Comparing the simulation results with the experimental data confirmed that the simulation successfully determined the optimised reaction conditions. The simplicity of the model, which considered only the initial catalyst activation period and derived rate constants from experimental data, likely contributed to its effectiveness. Further validation of the model using different photocatalysts is required to assess its reusability and robustness. Once validated, the model can be employed to compare the performance of modified photocatalysts, predict optimized reaction conditions, and further analyze reactor design aspects such as geometry and dimensions for larger-scale applications.

4. Conclusion

In this study, the application of CuO/BaTiO$_3$ for CO_2 photoreduction was investigated and compared to pristine BaTiO$_3$ and CuO impregnated on commercially available TiO$_2$ (Degussa P25) and ZnO. Among the catalyst samples tested, CuO/P25 exhibited the highest production of
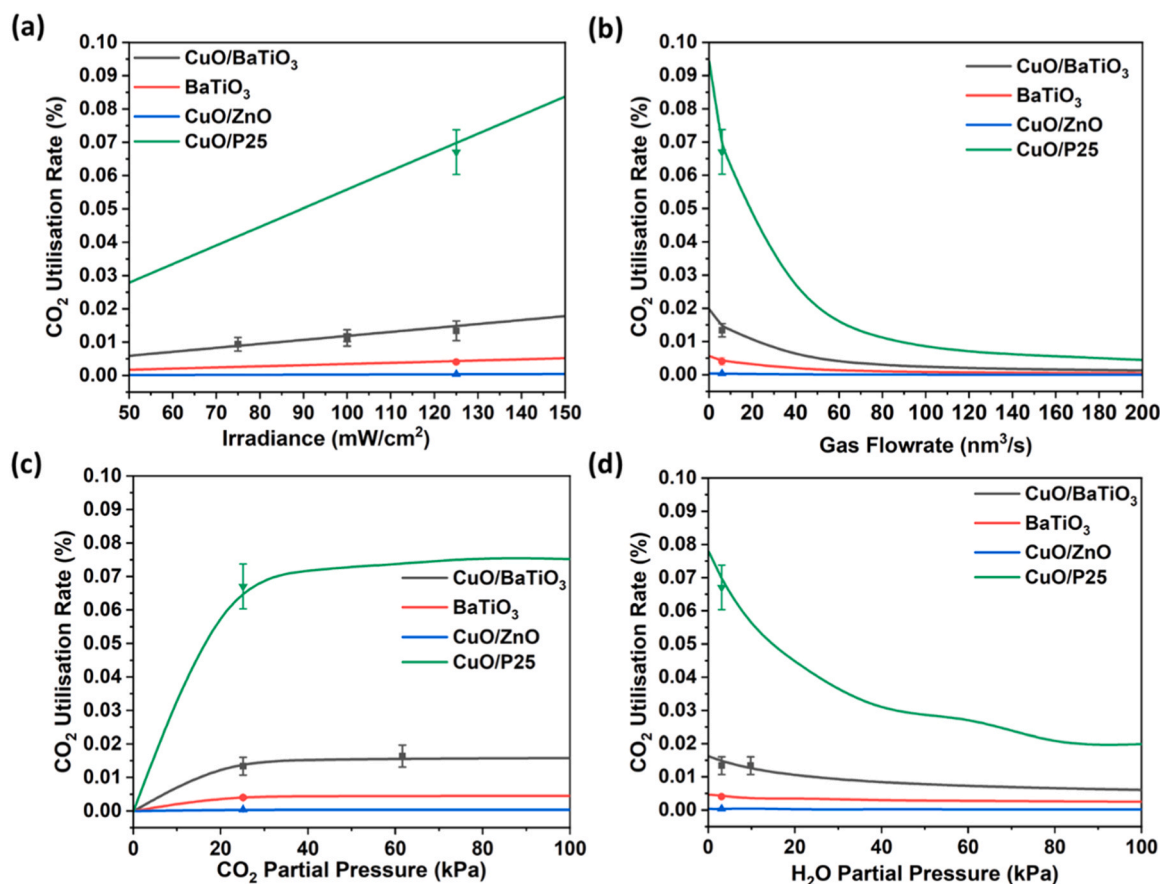
Fig. 9. Simulated patterns (Lines: green-CuO/P25, black - CuO/BaTiO$_3$, red - BaTiO$_3$, and blue - CuO/ZnO) for CO_2 utilisation rate influenced by (a) irradiance, (b) total gas flow rate, (c) H_2O partial pressure, (d) CO_2 partial pressure. The experimental results and confidence range (green triangle: CuO/P25, black square: CuO/ BaTiO$_3$, red circle: BaTiO$_3$, and blue triangle: CuO/ZnO) were plotted.

CH_4 (*i.e.*, 600 μmol $g_{catalyst}^{-1}$), while $CuO/BaTiO_3$ showed the highest production of CO (*i.e.*, 116 μmol $g_{catalyst}^{-1}$). The addition CuO as a co-catalyst ($CuO/BaTiO_3$, **φ_{CH4}: 0.1)** significantly improved the product selectivity towards CH_4 as evidenced by the higher quantum yield compared to pristine $BaTiO_3$ (**φ_{CH4}: 0.002).**

The systematic investigation of the process parameters, *i.e.*, irradiance, CO_2 and H_2O flow and partial pressure, and CO_2/H_2O ratio, on the product yield and selectivity were examined using DOE and CFD. The optimised reaction conditions determined from the experimental results were 125 mW cm^{-2}, 0.09 mL min^{-1} of CO_2, and 25 °C bubbler temperature. Compared to baseline conditions, the optimised condition gave a 2 and 10-fold increase in CO and CH_4 production, respectively. The results also indicated that a high CO_2:H_2O (30) and high irradiance condition (125 mW cm^{-2}) significantly favoured CH_4 production, whilst a low ratio (6) favoured CO production. Moreover, increasing the pressure of CO_2 led to an increase in the CO_2 utilisation rate up to an optimum while, increasing the partial pressure of H_2O showed the reverse effect.

CRediT authorship contribution statement

Ashween Kaur Virdee: Writing – original draft, Investigation, Formal analysis, Data curation, Software. **Irene Martin**: Writing – original draft, Investigation - Material synthesis, characterization and photoreduction tests. **Jeannie Z. Y. Tan**: Conceptualization, Methodology, Writing – review & editing. **Giulia Forghieri**: Reviewing. **M. Mercedes Maroto-Valer**: Supervision. **Michela Signoretto**: Supervision. **Mijndert Van der Spek**: Supervision, Writing – review & editing. **John M. Andresen**: Supervision, Writing – review & editing.

Declaration of Competing Interest

There are no conflicts to declare.

Data Availability

Data will be made available on request.

Appendix A. Supporting information

Supplementary data associated with this article can be found in the online version at doi:10.1016/j.jcou.2023.102568.

References

[1] K. Riahi, R. Schaeffer, J. Arango, K. Calvin, C. Guivarch, T. Hasegawa, K. Jiang, E. Kriegler, R. Matthews, G.P. Peters, A. Rao, S. Robertson, A.M. Sebbit, J. Steinberger, M. Tavoni, D.P. van Vuuren, Mitigation Pathways Compatible with Long-Term Goals. In IPCC, 2022: Climate Change 2022: Mitigation of Climate Change. Contribution of Working Group III to the Sixth Assessment Report of the Intergovernmental Panel on Climate Change, Cambridge, UK and New York, NY, USA, 2022.

[2] T.M. Gür, Carbon dioxide emissions, capture, storage and utilization: review of materials, processes and technologies, Prog. Energy Combust. Sci. 89 (2022), 100965, https://doi.org/10.1016/J.PECS.2021.100965.

[3] J.B. Wevers, L. Shen, M. van der Spek, What does it take to go net-zero-CO2? A life cycle assessment on long-term storage of intermittent renewables with chemical energy carriers, Front. Energy Res. 8 (2020) 1–18, https://doi.org/10.3389/fenrg.2020.00104.

[4] D. Sutter, M. van der Spek, M. Mazzotti, 110th anniversary: evaluation of CO2-based and CO2-free synthetic fuel systems using a Net-Zero-CO2-emission framework, Ind. Eng. Chem. Res. 58 (2019) 19958–19972, https://doi.org/10.1021/acs.iecr.9b00880.

[5] R. Peralta Muniz Moreira, G. Li Puma, Multiphysics computational fluid-dynamics (CFD) modeling of annular photocatalytic reactors by the discrete ordinates method (DOM) and the six-flux model (SFM) and evaluation of the contaminant intrinsic kinetics constants, Catal. Today 361 (2021) 77–84, https://doi.org/10.1016/J.CATTOD.2020.01.012.

[6] X. Lu, X. Luo, W.A. Thompson, J.Z.Y. Tan, M.M. Maroto-Valer, Investigation of carbon dioxide photoreduction process in a laboratory-scale photoreactor by computational fluid dynamic and reaction kinetic modeling, Front. Chem. Sci. Eng. 16 (2021) 1149–1163, https://doi.org/10.1007/S11705-021-2096-0.

[7] T.P. Nguyen, D.L.T. Nguyen, V.H. Nguyen, T.H. Le, D.V.N. Vo, Q.T. Trinh, S.R. Bae, S.Y. Chae, S.Y. Kim, Q.Van Le, Recent advances in TiO2-based photocatalysts for reduction of CO2 to fuels, Nanomaterials 10 (2020) 337, https://doi.org/10.3390/NANO10020337.

[8] C. Colbeau-Justin, Structural influence on charge-carrier lifetimes in TiO2 powders studied by microwave absorption, J. Mater. Sci. 38 (2003) 2429–2437, https://doi.org/10.1023/A:1023905102094.

[9] M. Shekofteh-Gohari, A. Habibi-Yangjeh, M. Abitorabi, A. Rouhi, Magnetically separable nanocomposites based on ZnO and their applications in photocatalytic processes: A review, Crit. Rev. Environ. Sci. Technol. 48 (2018) 806–857, https://doi.org/10.1080/10643389.2018.1487227.

[10] B.S. Kwak, M. Kang, Evaluation of photoreduction performance of CO2 to CH4 with H2O over alkaline-earth-metal-based peroskite nanoparticles, J. Nanosci. Nanotechnol. 17 (2017) 7351–7357, https://doi.org/10.1166/jnn.2017.14794.

[11] T. Watanabe, S.M. Khan, H. Kanoh, T. Ohba, Significant CO2 adsorption ability of nanoscale BaTiO3 ceramics fabricated by carbon-template-solvothermal reactions, Phys. Chem. Ind. J. 101 (2017) 1–9.

[12] J. Fujisawa, T. Eda, M. Hanaya, Comparative study of conduction-band and valence-band edges of TiO2, SrTiO3, and BaTiO3 by ionization potential measurements, Chem. Phys. Lett. 685 (2017) 23–26, https://doi.org/10.1016/j.cplett.2017.07.031.

[13] Y. Wang, C. Zhang, R. Li, Modulating the selectivity of photocatalytic CO2 reduction in barium titanate by introducing oxygen vacancies, Trans. Tianjin Univ. 28 (2022) 227–235, https://doi.org/10.1007/S12209-022-00334-X.

[14] X. Su, F. Meng, H. Tan, G. Chen, Unravelling the CO2 methanation mechanisms on a Ni-BaTiO3 catalyst: a theoretical investigation, J. CO2 Util. 64 (2022), 102170, https://doi.org/10.1016/J.JCOU.2022.102170.

[15] V.D.B.C. Dasireddy, B. Likozar, Photocatalytic CO2 reduction to methanol over bismuth promoted BaTiO3 perovskite nanoparticle catalysts, Renew. Energy 195 (2022) 885–895, https://doi.org/10.1016/J.RENENE.2022.06.064.

[16] Y.-Q. Cao, T.-Q. Zi, X.-R. Zhao, C. Liu, Q. Ren, J.-B. Fang, W.-M. Li, A.-D. Li, Enhanced visible light photocatalytic activity of Fe2O3 modified TiO2 prepared by atomic layer deposition, Sci. Rep. 10 (2020) 13437, https://doi.org/10.1038/s41598-020-70352-z.

[17] F. Conte, A. Villa, L. Prati, C. Pirola, S. Bennici, G. Ramis, I. Rossetti, Effect of metal cocatalysts and operating conditions on the product distribution and the productivity of the CO2 photoreduction, Ind. Eng. Chem. Res. 61 (2022) 2963–2972, https://doi.org/10.1021/acs.iecr.1c02514.

[18] M. Tahir, N.S. Amin, Photocatalytic CO2 reduction and kinetic study over In/TiO2 nanoparticles supported microchannel monolith photoreactor, Appl. Catal. A Gen. 467 (2013) 483–496, https://doi.org/10.1016/J.APCATA.2013.07.056.

[19] J. Wang, S. Lin, N. Tian, T. Ma, Y. Zhang, H. Huang, Nanostructured metal sulfides: classification, modification strategy, and solar-driven CO2 reduction application, Adv. Funct. Mater. 31 (2021) 2008008, https://doi.org/10.1002/ADFM.202008008.

[20] Y. Rambabu, U. Kumar, N. Singhal, M. Kaushal, M. Jaiswal, S.L. Jain, S.C. Roy, Photocatalytic reduction of carbon dioxide using graphene oxide wrapped TiO2 nanotubes, Appl. Surf. Sci. 485 (2019) 48–55, https://doi.org/10.1016/j.apsusc.2019.04.041.

[21] A. Meng, L. Zhang, B. Cheng, J. Yu, Dual cocatalysts in TiO2 photocatalysis, Adv. Mater. 31 (2019) 1807660, https://doi.org/10.1002/ADMA.201807660.

[22] M.A. Ávila-López, S. Gavrielides, X. Luo, A.E. Ojoajogwu, J.Z.Y. Tan, E. Luévano-Hipólito, L.M. Torres-Martínez, M.M. Maroto-Valer, Comparative study of CO2 photoreduction using different conformations of CuO photocatalyst: powder, coating on mesh and thin film, J. CO2 Util. 50 (2021), 101588, https://doi.org/10.1016/j.jcou.2021.101588.

[23] Y. Wang, S. Deng, B. Liu, Y. Jin, Mechanistic Understanding on the Role of Cu Species over the CuOx/TiO2 Catalyst for CO2 Photoreduction, ACS Omega 5 (2020) 18050–18063, https://doi.org/10.1021/ACSOMEGA.0C01533.

[24] T.P. Yendrapati Taraka, A. Gautam, S.L. Jain, S. Bojja, U. Pal, Controlled addition of Cu/Zn in hierarchical CuO/ZnO p-n heterojunction photocatalyst for high photoreduction of CO2 to MeOH, J. CO2 Util. 31 (2019) 207–214, https://doi.org/10.1016/J.JCOU.2019.03.012.

[25] W. Wang, L. Wang, W. Su, Y. Xing, Photocatalytic CO2 reduction over copper-based materials: a review, J. CO2 Util. 61 (2022), 102056, https://doi.org/10.1016/J.JCOU.2022.102056.

[26] W. Cai, X. Ma, J. Chen, R. Shi, Y. Wang, Y. Yang, D. Jing, H. Yuan, J. Du, M. Que, Synergy of oxygen vacancy and piezoelectricity effect promotes the CO_2 photoreduction by BaTiO3, Appl. Surf. Sci. 619 (2023), 156773, https://doi.org/10.1016/J.APSUSC.2023.156773.

[27] S. Joshi, R.K. Canjeevaram Balasubramanyam, S.J. Ippolito, Y.M. Sabri, A. E. Kandjani, S.K. Bhargava, M.V. Sunkara, Straddled band aligned CuO/BaTiO3 heterostructures: role of energetics at nanointerface in improving photocatalytic and CO_2 sensing performance, ACS Appl. Nano Mater. 1 (2018) 3375–3388, https://doi.org/10.1021/ACSANM.8B00583.

[28] A. Olivo, W.A. Thompson, E.R.B. Bay, E. Ghedini, F. Menegazzo, M. Maroto-Valer, M. Signoretto, Investigation of process parameters assessment via design of experiments for CO_2 photoreduction in two photoreactors, J. CO_2 Util. 36 (2020) 25–32, https://doi.org/10.1016/j.jcou.2019.10.009.

[29] A. Olivo, D. Zanardo, E. Ghedini, F. Menegazzo, M. Signoretto, Solar Fuels by heterogeneous photocatalysis: from understanding chemical bases to process development, ChemEngineering 2 (2018) 42, https://doi.org/10.3390/chemengineering2030042.

[30] W.A. Thompson, E. Sanchez Fernandez, M.M. Maroto-Valer, Probability langmuir-hinshelwood based CO_2 photoreduction kinetic models, Chem. Eng. J. 384 (2020), 123356, https://doi.org/10.1016/j.cej.2019.123356.

[31] M. Dilla, R. Schlögl, J. Strunk, Photocatalytic CO_2 reduction under continuous flow high-purity conditions: quantitative evaluation of CH4 formation in the steady-state, ChemCatChem 9 (2017) 696–704, https://doi.org/10.1002/CCTC.201601218.

[32] G.L. Chiarello, D. Ferri, E. Selli, Effect of the CH3OH/H2O ratio on the mechanism of the gas-phase photocatalytic reforming of methanol on noble metal-modified TiO2, J. Catal. 280 (2011) 168–177, https://doi.org/10.1016/j.jcat.2011.03.013.

[33] J. Oliveira De Brito Lira, H.G. Riella, N. Padoin, C. Soares, An overview of photoreactors and computational modeling for the intensification of photocatalytic processes in the gas-phase: state-of-art, J. Environ. Chem. Eng. 9 (2021), 105068, https://doi.org/10.1016/J.JECE.2021.105068.

[34] F. Griesmer, Modeling Chemical Reactions: Kinetics | COMSOL Blog, (2013). https://www.comsol.com/blogs/modeling-chemical-reactions-kinetics/ (accessed June 16, 2022).

[35] X. Lu, X. Luo, J.Z.Y. Tan, M.M. Maroto-Valer, Simulation of CO_2 photoreduction in a twin reactor by multiphysics models, Chem. Eng. Res. Des. 171 (2021) 125–138, https://doi.org/10.1016/J.CHERD.2021.04.011.

[36] Y. Boyjoo, M. Ang, V. Pareek, CFD simulation of a pilot scale slurry photocatalytic reactor and design of multiple-lamp reactors, Chem. Eng. Sci. 111 (2014) 266–277, https://doi.org/10.1016/J.CES.2014.02.022.

[37] K. Yuan, L. Yang, X. Du, Y. Yang, Performance analysis of photocatalytic CO_2 reduction in optical fiber monolith reactor with multiple inverse lights, Energy Convers. Manag. 81 (2014) 98–105, https://doi.org/10.1016/J.ENCONMAN.2014.02.027.

[38] S. Corbel, G. Charles, N. Becheikh, T. Roques-Carmes, O. Zahraa, Modelling and design of microchannel reactor for photocatalysis, Virtual Phys. Prototyp. 7 (2012) 203–209, https://doi.org/10.1080/17452759.2012.708837.

[39] S.W. Verbruggen, M. Keulemans, J. van Walsem, T. Tytgat, S. Lenaerts, S. Denys, CFD modeling of transient adsorption/desorption behavior in a gas phase photocatalytic fiber reactor, Chem. Eng. J. 292 (2016) 42–50, https://doi.org/10.1016/J.CEJ.2016.02.014.

[40] X. Lu, J.Z.Y. Tan, M.M. Maroto-Valer, Investigation of CO 2 photoreduction in an annular fluidized bed photoreactor by MP-PIC simulation, Ind. Eng. Chem. Res. 61 (2022) 3123–3136, https://doi.org/10.1021/ACS.IECR.1C04035.

[41] C.S. Ribeiro, J.Z.Y. Tan, M.M. Maroto-Valer, M.A. Lansarin, Photocatalytic reduction of CO_2 over Bi2WO6 in a continuous-flow differential photoreactor: investigation of operational parameters, J. Environ. Chem. Eng. 9 (2021), 105097, https://doi.org/10.1016/j.jece.2021.105097.

[42] W.A. Thompson, A. Olivo, D. Zanardo, G. Cruciani, F. Menegazzo, M. Signoretto, M.M. Maroto-Valer, Systematic study of TiO2/ZnO mixed metal oxides for CO_2 photoreduction, RSC Adv. 9 (2019) 21660–21666, https://doi.org/10.1039/c9ra03435h.

[43] M. Chandrasekar, M. Subash, S. Logambal, G. Udhayakumar, R. Uthrakumar, C. Inmozhi, W.A. Al-Onazi, A.M. Al-Mohaimeed, T.W. Chen, K. Kanimozhi, Synthesis and characterization studies of pure and Ni doped CuO nanoparticles by hydrothermal method, J. King Saud. Univ. Sci. 34 (2022), 101831, https://doi.org/10.1016/j.jksus.2022.101831.

[44] W.A. Thompson, C. Perier, M.M. Maroto-Valer, Systematic study of sol-gel parameters on TiO2 coating for CO_2 photoreduction, Appl. Catal. B. 238 (2018) 136–146, https://doi.org/10.1016/j.apcatb.2018.07.018.

[45] O. Ola, M.M. Maroto-Valer, Review of material design and reactor engineering on TiO2 photocatalysis for CO_2 reduction, J. Photochem. Photobiol. C. 24 (2015) 16–42, https://doi.org/10.1016/J.JPHOTOCHEMREV.2015.06.001.

[46] A. Virdee, J. Andresen, Advances in design and scale-up of solar fuel systems, in: N. D. Sankir, M. Sankir (Eds.), Solar Fuels, John Wiley & Sons, Ltd, 2023, pp. 247–283, https://doi.org/10.1002/9781119752097.CH8.

[47] Y. Boyjoo, H. Sun, J. Liu, V.K. Pareek, S. Wang, A review on photocatalysis for air treatment: From catalyst development to reactor design, Chem. Eng. J. 310 (2017) 537–559, https://doi.org/10.1016/J.CEJ.2016.06.090.

[48] Y. Boyjoo, M. Ang, V. Pareek, Some aspects of photocatalytic reactor modeling using computational fluid dynamics, Chem. Eng. Sci. 101 (2013) 764–784, https://doi.org/10.1016/J.CES.2013.06.035.

[49] Y. Ji, Y. Luo, Theoretical study on the mechanism of photoreduction of CO_2 to CH4 on the anatase TiO2 (101) surface, ACS Catal. 6 (2016) 2018–2025, https://doi.org/10.1021/acscatal.5b02694.

[50] A.H. Jawad, N.S.A. Mubarak, M.A.M. Ishak, K. Ismail, W.I. Nawawi, Kinetics of photocatalytic decolourization of cationic dye using porous TiO2 film, J. Taibah Univ. Sci. 10 (2016) 352–362, https://doi.org/10.1016/j.jtusci.2015.03.007.

[51] K.P. Sundar, S. Kanmani, Progression of Photocatalytic reactors and it's comparison: a review, Chem. Eng. Res. Des. 154 (2020) 135–150, https://doi.org/10.1016/j.cherd.2019.11.035.

[52] K.V. Kumar, K. Porkodi, F. Rocha, Langmuir–Hinshelwood kinetics – a theoretical study, Catal. Commun. 9 (2008) 82–84, https://doi.org/10.1016/j.catcom.2007.05.019.

[53] J.Z. Bloh, A holistic approach to model the kinetics of photocatalytic reactions, Front. Chem. 7 (2019), 128, https://doi.org/10.3389/fchem.2019.00128.

[54] W.A. Thompson, E.S. Fernandez, M.M. Maroto-Valer, Review and analysis of CO_2 photoreduction kinetics, ACS Sustain. Chem. Eng. 8 (2020) 4677–4692, https://doi.org/10.1021/ACSSUSCHEMENG.9B06170.

[55] H. Kisch, D. Bahnemann, Best practice in photocatalysis: comparing rates or apparent quantum yields? J. Phys. Chem. Lett. 6 (2015) 1907–1910, https://doi.org/10.1021/acs.jpclett.5b00521.

[56] W.L. Zhong, Y.G. Wang, P.L. Zhang, B.D. Qu, Phenomenological study of the size effect on phase transitions in ferroelectric particles, Phys. Rev. B. 50 (1994) 698–703, https://doi.org/10.1103/PhysRevB.50.698.

[57] B. Yang, Y. Ai, Facile fabrication of CuO nanosheets and in situ transmission electron microscopy/X-ray diffraction heating characterization of microstructure evolution, Phys. Status Solidi (A 219 (2022) 2100617, https://doi.org/10.1002/pssa.202100617.

[58] V. Bansal, P. Poddar, A. Ahmad, M. Sastry, Room-temperature biosynthesis of ferroelectric barium titanate nanoparticles, J. Am. Chem. Soc. 128 (2006) 11958–11963, https://doi.org/10.1021/ja063011m.

[59] K. Siemek, A. Olejniczak, L.N. Korotkov, P. Konieczny, A.V. Belushkin, Investigation of surface defects in BaTiO3 nanopowders studied by XPS and positron annihilation lifetime spectroscopy, Appl. Surf. Sci. 578 (2022), 151807, https://doi.org/10.1016/j.apsusc.2021.151807.

[60] S. Nayak, B. Sahoo, T.K. Chaki, D. Khastgir, Facile preparation of uniform barium titanate (BaTiO3) multipods with high permittivity: impedance and temperature dependent dielectric behavior, RSC Adv. 4 (2014) 1212–1224, https://doi.org/10.1039/C3RA44815K.

[61] H. Bantawal, D. Krishna Bhat, Hierarchical porous Batio3 nano-hexagons as a visible light photocatalyst, Int. J. Eng. Technol. 7 (2018) 105, https://doi.org/10.14419/ijet.v7i4.5.20022.

[62] T.-M. Usher, B. Kavey, G. Caruntu, K. Page, Effect of BaCO3 impurities on the structure of BaTiO3 nanocrystals: implications for multilayer ceramic capacitors, ACS Appl. Nano Mater. 3 (2020) 9715–9723, https://doi.org/10.1021/acsanm.0c01809.

[63] H.H. Nguyen, G. Gyawali, T.H. Kim, S. Bin Humam, S.W. Lee, Blue TiO2 polymorph: an efficient material for dye-sensitized solar cells fabricated using a low-temperature sintering process, Prog. Nat. Sci.: Mater. Int. 28 (2018) 548–553, https://doi.org/10.1016/j.pnsc.2018.08.003.

[64] R. Al-Gaashani, S. Radiman, A.R. Daud, N. Tabet, Y. Al-Douri, XPS and optical studies of different morphologies of ZnO nanostructures prepared by microwave methods, Ceram. Int. 39 (2013) 2283–2292, https://doi.org/10.1016/j.ceramint.2012.08.075.

[65] Minitab 21 Support, Effects plots for Analyze Factorial Design, (2022). ⟨https://support.minitab.com/en-us/minitab/21/help-and-how-to/statistical-modeling/doe/how-to/factorial/analyze-factorial-design/interpret-the-results/all-statistics-and-graphs/effects-plots/⟩ (accessed December 1, 2022).

[66] B.S. Kwak, J.Y. Do, N.K. Park, M. Kang, Surface modification of layered perovskite Sr2TiO4 for improved CO_2 photoreduction with H2O to CH4, Sci. Rep. 7 (1) (2017) 15, https://doi.org/10.1038/s41598-017-16605-w.

[67] M. Dilla, A. Mateblowski, S. Ristig, J. Strunk, Photocatalytic CO_2 reduction under continuous flow high-purity conditions: influence of light intensity and H2O concentration, ChemCatChem 9 (2017) 4345–4352, https://doi.org/10.1002/CCTC.201701189.

[68] N.M. Dimitrijevic, B.K. Vijayan, O.G. Poluektov, T. Rajh, K.A. Gray, H. He, P. Zapol, Role of water and carbonates in photocatalytic transformation of CO 2 to CH4 on titania, J. Am. Chem. Soc. 133 (2011) 3964–3971, https://doi.org/10.1021/JA108791U.

[69] A. Adamu, M. Isaacs, K. Boodhoo, F.R. Abegão, Investigation of Cu/TiO2 synthesis methods and conditions for CO_2 photocatalytic reduction via conversion of bicarbonate/carbonate to formate, J. CO_2 Util. 70 (2023), 102428, https://doi.org/10.1016/J.JCOU.2023.102428.